Astronomy & Astrophysics

THE THREE HUNDRED project: Estimating the dependence of gas filaments on the mass of galaxy clusters

Sara Santoni[1,2,3,*], Marco De Petris[1], Gustavo Yepes[2,4], Antonio Ferragamo[1,5], Matteo Bianconi[6], Meghan E. Gray[6], Ulrike Kuchner[6], Frazer R. Pearce[6], Weiguang Cui[2,4,7], and Stefano Ettori[8,9]

[1] Dipartimento di Fisica, Sapienza Università di Roma, Piazzale Aldo Moro 5, I-00185 Rome, Italy
[2] Departamento de Física Teórica, Facultad de Ciencias, Universidad Autónoma de Madrid, Modulo 8, E-28049 Madrid, Spain
[3] Escuela de Doctorado UAM, Centro de Estudios de Posgrado, Universidad Autónoma de Madrid, E-28049 Madrid, Spain
[4] Centro de Investigación Avanzada en Física Fundamental (CIAFF), Facultad de Ciencias, Universidad Autónoma de Madrid, E-28049 Madrid, Spain
[5] Dipartimento di Fisica Ettore Pancini, Università degli Studi di Napoli Federico II, Via Cintia 21, I-80126 Napoli, Italy
[6] School of Physics and Astronomy, University of Nottingham, Nottingham NG7 2RD, UK
[7] Institute for Astronomy, University of Edinburgh, Edinburgh EH9 3HJ, UK
[8] INAF, Osservatorio di Astrofisica e Scienza dello Spazio, Via Piero Gobetti 93/3, I-40129 Bologna, Italy
[9] INFN, Sezione di Bologna, Viale Berti Pichat 6/2, I-40127 Bologna, Italy

ABSTRACT

Context. Galaxy clusters are located in the densest areas of the universe and are intricately connected to larger structures through the filamentary network of the cosmic web. In this scenario, matter flows from areas of lower density to higher density. As a result, the properties of galaxy clusters are deeply influenced by the filaments that are attached to them, which are quantified by a parameter known as connectivity.
Aims. We explore the dependence of gas-traced filaments connected to galaxy clusters on the mass and dynamical state of the cluster. Moreover, we evaluate the effectiveness of the cosmic web extraction procedure from the gas density maps of simulated cluster regions.
Methods. Using the DisPerSE cosmic web finder, we identify filamentary structures from the 3D gas particle distribution in 324 simulated regions of $30\,h^{-1}$ Mpc side from THE THREE HUNDRED hydrodynamical simulation at redshifts $z = 0$, 1, and 2. We estimate the connectivity at various apertures for ∼3000 groups and clusters spanning a mass range from $10^{13}\,h^{-1}\,M_\odot$ to $10^{15}\,h^{-1}\,M_\odot$. Relationships between connectivity and cluster properties like radius, mass, dynamical state, and hydrostatic mass bias are explored.
Results. We show that the connectivity is strongly correlated with the mass of galaxy clusters, with more massive clusters being on average more connected. This finding aligns with previous studies in the literature, both from observational and simulated datasets. Additionally, we observe a dependence of the connectivity on the aperture at which it is estimated. We find that connectivity decreases with cosmic time, while no dependencies on the dynamical state and hydrostatic mass bias of the cluster are found. Lastly, we observe a significant agreement between the connectivity measured from gas-traced and mock-galaxy-traced filaments in the simulation.

Key words. methods: numerical – methods: statistical – galaxies: clusters: general – large-scale structure of Universe

1. Introduction

Clusters of galaxies, considered the largest gravitationally bound structures in the universe, are located at the nodes of an intricate web-like structure known as the 'cosmic web' (Bond et al. 1996). This cosmic pattern of dark matter (DM) and baryons and the formation of large-scale structures are predicted as a consequence of the non-linear growth of primordial density perturbations (Zel'dovich 1970; Peebles 1980). In this framework, matter flows from underdense regions to overdense structures, resulting in compact galaxy clusters at the nodes of elongated filamentary structures and filaments at the intersection of sheet-like formations, known as walls, surrounded by vast void regions.

The cosmic web has been observed by several galaxy surveys, such as the Sloan Digital Sky Survey (SDSS; York et al. 2000) and the 2dF Galaxy Redshift Survey (2dFGRS; Colless et al. 2001). Furthermore, the properties of the cosmic web and its components have been identified through several large-scale numerical simulations, both N-body and hydrodynamical, such as the Millennium simulation (Springel 2005), the MilleniumTNG project (Hernández-Aguayo et al. 2023), the Illustris project (Vogelsberger et al. 2014), IllustrisTNG (Nelson et al. 2019), the EAGLE project (Schaye et al. 2015), and the SIMBA project (Davé et al. 2019).

Depending on the scientific goal of the study, different features of the cosmic web can be examined, often without relying on unequivocal definitions. Consequently, several algorithms have been developed to identify the cosmic web, some tailored for simulations and others for observational data, as is illustrated in the exhaustive review by Libeskind et al. (2018). The different algorithms generally converge on the identification and characterisation of specific features, but they reflect the complexity involved in the study and definitions of these structures.

In particular, the most used extraction methods can be grouped as graph and percolation techniques (e.g. MST, Alpaslan et al. 2014 and T-Rex, Bonnaire et al. 2020), stochastic

---

* Corresponding author; sara.santoni@uniroma1.it

methods (e.g. Bisous model, Tempel et al. 2016), methods based on the Hessian of the density, tidal, or velocity fields (e.g. T-web, Forero-Romero et al. 2009, V-web, Hoffman et al. 2012), and, among these, those that follow a multi-scale approach (e.g. MMF, Aragón-Calvo et al. 2007, NEXUS and NEXUS+, Cautun et al. 2013). Moreover, the cosmic web can be identified with topological methods (e.g. Spineweb, Aragón-Calvo et al. 2010a and DisPerSE, Sousbie 2011; Sousbie et al. 2011) and, lastly, phase-space methods (e.g. ORIGAMI, Falck et al. (2012).

In addition to the galaxy clusters, filaments constitute the densest regions of the cosmic web, containing approximately 50% of the matter in the universe (Cautun et al. 2014). Filaments serve an important function in the accretion phase of galaxy clusters, acting as pathways for matter transportation towards the centre of the node to which they are connected. The connectivity of the cosmic web, which measures the number of filaments connected to a cluster, offers a method of quantifying the interaction between clusters and the filaments surrounding them, enabling the assessment of structural evolution (Codis et al. 2018). Several works in the literature have been investigating the correlation between connectivity and a cluster's properties, such as its mass and its dynamical state (see e.g. Darragh Ford et al. 2019; Sarron et al. 2019; Malavasi et al. 2020b; Gouin et al. 2021; Galárraga-Espinosa et al. 2024).

Furthermore, several studies proved that filaments play a significant role in the so-called 'pre-processing' of the galaxies that reside within the filamentary structures. Filaments affect galaxy evolution and galaxy properties, before entering the cluster, through several processes as ram-pressure, tidal effects, and mergers (see the reviews of Boselli & Gavazzi 2006, 2014 and more recent works e.g. Kraljic et al. 2018; Winkel et al. 2021; Hellwing et al. 2021; Song et al. 2021; Donnan et al. 2022; Kotecha et al. 2022; Kuchner et al. 2022; Malavasi et al. 2022; Galárraga-Espinosa et al. 2024; Bulichi et al. 2024). Therefore, the outskirts of clusters provide a distinctive environment for examining matter accretion dynamics and galaxy properties.

Unlike the galaxy content of filaments, which has been extensively identified with galaxy surveys, the detection of the gas component has proven more challenging. Hydrodynamical simulations (see e.g. Bond et al. 1996; Davé et al. 2001; Shull et al. 2012; Tuominen et al. 2021) predict that the filamentary structures of the cosmic web host a large fraction of the missing baryons[1] in a low-density and warm-hot state known as the warm-hot intergalactic medium (WHIM), with a density of $\delta_b \approx 10-100$ and a temperature in the range of 10^5-10^7 K.

The hot phase of WHIM, with $\log T(K) \approx 5.5-7$, is not observable through absorption, being fully ionised, contrary to the low-temperature phase, with $\log T(K) \approx 5-5.5$, which has been detected several times through metal absorption lines (Danforth et al. 2016). Despite having a faint emission, several attempts have been made to detect the warmest phase of WHIM through direct X-ray observations (see e.g. Eckert et al. 2015; Nicastro et al. 2018 and the Sunyaev-Zel'dovich effect, employing stacking methods (Tanimura et al. 2019, 2020, 2022) or looking at the densest regions between two close galaxy clusters (Bonjean et al. 2018; Hincks et al. 2022).

In this work, we use the outputs of THE THREE HUNDRED (Cui et al. 2018a) hydrodynamical simulations to extract the cosmic web in the surrounding volumes of galaxy clusters, with a specific focus on the filamentary structures, from the gas particle distribution using the cosmic web finder DisPerSE. By analysing the connectivity estimates of simulated galaxy clusters, this investigation explores the influence of filaments on the main properties of galaxy clusters, such as their mass and dynamical state, and assesses the cosmic web extraction from diffuse gas particles within the simulated THE THREE HUNDRED regions.

This paper is structured as follows. Sect. 2 provides a detailed overview of THE THREE HUNDRED simulation and the theoretical framework behind the cosmic web finder DisPerSE. The process of creating the gas density maps and calibrating DisPerSE is discussed in Sect. 3. In Sect. 4, we present the results of the connectivity analysis, while in Sect. 5 we investigate the effect of cosmic web tracers by comparing the gas-traced filaments to mock-galaxy-traced filaments. Finally, Sect. 6 summarises the main results of our study.

2. Simulation and methods

2.1. THE THREE HUNDRED project

The dataset analysed in this work was extracted from THE THREE HUNDRED project[2] (Cui et al. 2018a). THE THREE HUNDRED hydrodynamical simulation consists of 324 zoom-in re-simulated regions centred on the most massive haloes selected at $z = 0$ from the MultiDark Planck 2 (hereafter as MDPL2) simulation (Klypin et al. 2016). MDPL2 is a DM-only cosmological simulation, consisting of a periodic cube with a side length of $1\,h^{-1}$ Gpc with 3840^3 DM particles, each with a mass of $1.5 \times 10^9\,h^{-1}\,M_\odot$. The cosmological parameters used in MDPL2 and THE THREE HUNDRED are those reported in the 2015 *Planck* data release (Planck Collaboration XIII 2016) ($h = 0.678$, $n_s = 0.96$, $\sigma_8 = 0.823$, $\Omega_\Lambda = 0.693$, $\Omega_M = 0.307$, and $\Omega_B = 0.048$).

The 324 spherical regions of THE THREE HUNDRED, centred on the most massive haloes ($M_{vir} > 8 \times 10^{14}\,h^{-1}\,M_\odot$), have a radius of $15\,h^{-1}$ Mpc. The DM particles within these regions are split into separate DM and gas particles, according to the cosmological baryonic mass fraction, with masses of $m_{DM} = 12.7 \times 10^8\,h^{-1}\,M_\odot$ and $m_{gas} = 2.36 \times 10^8\,h^{-1}\,M_\odot$.

In this analysis, we have used the regions re-simulated with the smoothed particle hydrodynamics (SPH) code GADGET-X (Springel 2005; Beck et al. 2016) – a modified version of the GADGET3 code – which implements radiative cooling and star formation (Springel & Hernquist 2003), chemical stellar evolution (Tornatore et al. 2007), supermassive black hole (BH) accretion, and active galactic nuclei and supernovae feedback (Steinborn et al. 2015). The haloes and subhaloes within each region were identified with the publicly available[3] Amiga Halo Finder (AHF; Knollmann & Knebe 2011), which includes DM, gas, stars, and BHs in the density peak finding process and estimates the co-ordinates and properties of the clusters, such as their mass, radius, and luminosities at various overdensities. The simulation runs are stored in 129 snapshots, from redshift $z = 17$ to $z = 0$. In this work, we analyse the galaxy clusters' catalogues at redshifts $z = 0$, $z = 1.03$, and $z = 2.02$, which span, at $z = 0$, a mass range of $10^{13} \leq M_{200}\,h^{-1}\,M_\odot \leq 2.62 \times 10^{15}$.

---

[1] When compared to the concordance cosmology model, we observe a ≈30% deficit in the census of observed baryons from low-redshift sources, such as galaxies, groups, and clusters, in the intergalactic and circumgalactic medium.

---

[2] https://the300-project.org
[3] http://popia.ft.uam.es/AHF/

2.2. DisPerSE

The cosmic web in the simulated regions was extracted using the publicly available[4] Discrete Persistent Structure Extractor (DisPerSE; Sousbie 2011; Sousbie et al. 2011). DisPerSE is a topological structure finder, designed to identify multi-scale structures. It relies on discrete morse theory (Forman 1998; Gyulassy et al. 2008) to identify the critical points of density fields. The noise introduced into the detection by the finite sampling of the density field was reduced with the approach of persistent homology theory (Edelsbrunner et al. 2002) and topological simplification (Edelsbrunner et al. 2002; Gyulassy et al. 2008).

In short, from a given 2D or 3D distribution of tracers, DisPerSE provides the position of the extreme points – where the gradient of the field is null – and the integral lines that connect them, which form the filaments. The starting point of DisPerSE can either be a catalogue of the tracers' co-ordinates (e.g. galaxies or haloes) or a pixelated density map, as is used in this work. In the first case, the density field is extracted from the Delaunay tessellation of the distribution with the Delaunay tessellation field estimator (DTFE; Schaap & van de Weygaert 2000; van de Weygaert & Schaap 2009).

From the density field, the identified extreme points were classified as maxima, minima, saddle, and bifurcation points; that is, where a filament splits in two. The ridges were presented as a set of segments that connect two extreme points – usually a maximum and a saddle point – following the density field. The robustness of filaments – that is, their reliability – was quantified through a threshold parameter called 'persistence cut', defined as the absolute difference in the density value of the two critical points at the filament's extremes. The choice of the persistence allows for low-significance and noisy structures to be filtered out.

3. Cosmic web extraction

3.1. DisPerSE calibration

In order to extract a significant filamentary skeleton from the density distribution, a combination of parameters – the Gaussian smoothing of the input density map and the persistence cut of DisPerSE – needs to be tuned. The first step of the cosmic web extraction is the smoothed gas density field reconstructed from the regions of the hydrodynamical simulation. The Three Hundred gas-traced cosmic web has been widely analysed in previous works; namely, to study the properties of filaments (Rost et al. 2021, 2024) and as a benchmark for the identification of galaxy-traced filaments (Kuchner et al. 2020, 2021). In this work, we have chosen to analyse the filamentary structures traced from the gas particle distribution because we plan, in future studies, to use 3D gas filaments and their projection as a benchmark for the detection of filaments from mock Compton-y maps generated in The Three Hundred simulation, as is described in Cui et al. (2018a).

The gas particles of each simulated region were first binned in a 3D grid of $30\,h^{-1}$ Mpc per side, with a pixel resolution of $150\,h^{-1}$ kpc. Then, to avoid sharp variations from one pixel to another, we applied a Gaussian kernel to smooth the density field. As the smoothing kernel of the map increases, only the more distinct structures will be identified by the filament finder, leading to a network that only features robust critical points and

filaments. For this analysis, we applied a Gaussian kernel with a full width at half maximum (FWHM) of 4 pixels, equivalent to $600\,h^{-1}$ kpc. We opted for this specific kernel size, ensuring it remains smaller than the diameter of the galaxy clusters that we analysed, to preserve the resolution of these structures, as is shown in Fig. 1, where we compare the chosen value and two larger smoothing kernels to the distribution of the diameters of clusters at $z = 0$.

In addition to the smoothing level of the density map, the robustness of the extracted network depends also on the DisPerSE parameter 'persistence'. The effect of the persistence cut on the network is similar to the Gaussian smoothing, with higher values of persistence leading to less critical point pairs, and therefore to the removal of less significant filaments. The optimal value of persistence cut for our dataset is 0.5, which identifies the threshold between significant topological features and noisy ones, as is seen in the DisPerSE Persistence Diagram Viewer (`pdview`), accessible with option `-interactive` of the function `mse`. The persistence cut differs from the commonly referenced persistence ratio, expressed as a number of standard deviation σ and defined as the ratio of the values of the points in a critical pair. The persistence ratio is often applied to a density field of discrete catalogues (e.g. computed using DTFE). The persistence absolute cut of 0.5 that we apply to 3D gas density maps is comparable to a persistence ratio of 8.5σ, producing filament skeletons that look visually similar.

The density maps were first analysed by DisPerSE with the function `mse`, with the options `-forceLoops`, `-periodicity 000`, `-cut 0.5`, and `-upSkl`, to compute the Morse-smale complexes. During this step, the filaments were extracted and the critical points were identified. Then, the networks were post-treated with the function `skelconv`, which we implemented with the following options: `-smooth 1`, `-breakdown`, `-rmOutside`, and `-rmBoundary`. Here, the option `-breakdown` merges the infinitely close pieces of arcs and adds the bifurcations points, while the `-smooth` option determines the straightness of the filament's trace, while keeping the critical points' co-ordinates fixed. We note that the `-smooth` function does not affect the extraction and positions of filamentary structures and, although it has a similar name, it is different from the Gaussian smoothing kernel applied to the density maps, which operates on the density field prior to the cosmic web extraction procedure on DisPerSE.

3.2. Simulated cosmic web network

In the DisPerSE output networks, the galaxy groups and clusters are defined only by the co-ordinates of the maxima (the nodes), while the filaments are defined only by the position of their spines. To associate the extracted skeleton with the density distribution of the simulation, one needs to match the nodes to The Three Hundred galaxy clusters, identified with AHF. While there are several ways to associate the nodes with clusters (for a complete study we refer the reader to Cohn 2022), in this analysis we required the distance between the co-ordinates of the node and the cluster to be less than the smoothing kernel of 4 pixels. Where multiple pairs satisfied this condition, we matched the DisPerSE node to the nearest AHF cluster.

To evaluate the accuracy of the DisPerSE catalogue and of the matches, we can compute the completeness of the sample, defined as the number of groups and clusters matched to nodes, normalised by the total number of groups, as in Cornwell et al. (2024). The completeness depends on the smoothing scale of the density maps, with a larger and less filtering smoothing kernel
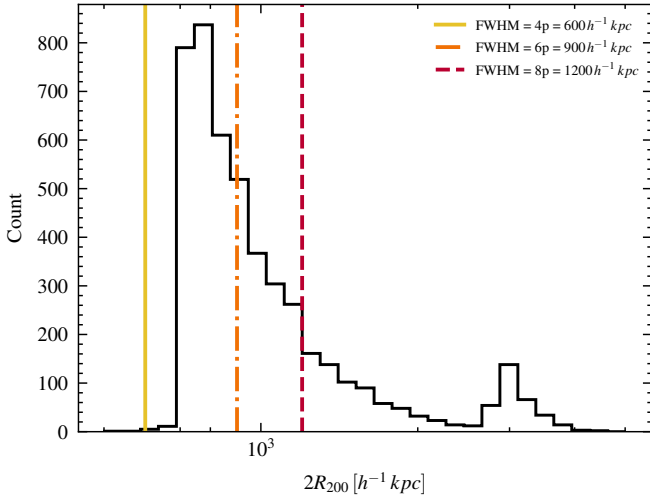

Fig. 1. Diameter $2R_{200}$ distribution of galaxy clusters at $z = 0$. The vertical lines represent the smoothing kernel FWHM at 4, 6, and 8 pixels, respectively, in yellow (solid), orange (dash-dotted), and red (dashed).

Fig. 2. Completeness of the sample. Each dot refers to the completeness of the sample, averaged over the 324 simulated regions, extracted with different smoothing kernels. The error bars represent the standard deviation error.

resulting in lower completeness of the sample, as is shown in Fig. 2. Here, we display the completeness of the sample as a function of the Gaussian smoothing FWHM, averaged over the 324 simulated regions. To test only the effect of the smoothing scale on the completeness of the sample, we used the same persistence cut for all the smoothing values, which alters the skeleton in a similar way to the smoothing. This result agrees with Cohn (2022) and Galárraga-Espinosa et al. (2024), where they studied the effect of the smoothing on the completeness of skeletons extracted from DM and galaxy distributions, respectively.

The sample analysed in this work has an average completeness value of 89%, indicating that almost every group or cluster identified in the simulated regions has a matched DisPerSE node. It is worth noticing that since the completeness is lower than the ideal value of 100%, some clusters remain unmatched by any DisPerSE nodes. This discrepancy might be attributed to their co-ordinates' distance exceeding the threshold we set. This phenomenon could be explained by considering that DisPerSE node co-ordinates are determined solely from the gas-only density distribution, unlike cluster co-ordinates, which also incorporate data from DM particles. Therefore, the different spatial distributions of DM and gas particles near the centre of the regions could affect the peak density finding process (Cui et al. 2018b; Lokken et al. 2023). Conversely, there are DisPerSE nodes without any corresponding clusters. This population of nodes likely represents local maximum points of the density field not classified as haloes by AHF or nodes associated with sub-haloes. To avoid possible contamination by low-resolution DM particles near the borders, we considered only the matched nodes inside a sphere of $13\,h^{-1}$ Mpc radius from the centre of each region. Lastly, we note that the galaxy groups and clusters analysed in this work – except the 324 most massive ones – reside within the $15\,h^{-1}$ Mpc environment of very massive galaxy clusters ($M_{\mathrm{vir}} > 8 \times 10^{14}\,h^{-1}\,M_\odot$).

The final sample used for this analysis, including all the 324 simulated regions, amounts to 3412 galaxy groups and clusters and 12 643 filaments at $z = 0$. The filament sample includes filaments going from a maximum point to another – with a saddle point in the middle – filaments from one maximum point to a bifurcation point and filaments with two bifurcation points at the extremes. The filame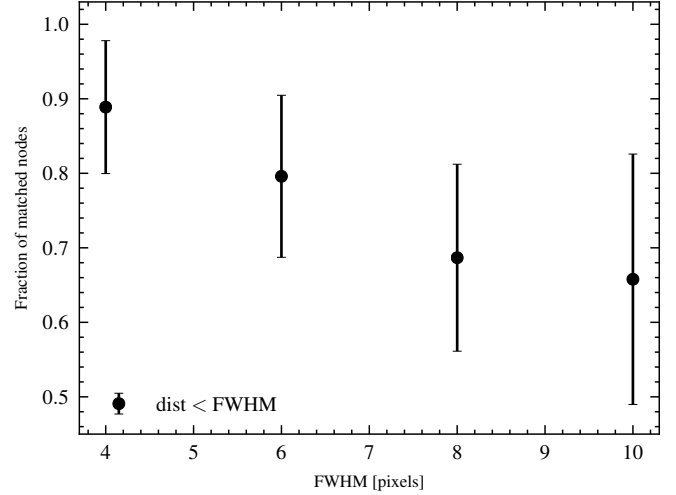nt length distribution, computed as the sum of the lengths of all segments belonging to each filament, is shown in Fig. 3, along with the median values of the distribution. We plot the length distribution of the whole sample in black, the length distribution of maximum-maximum filaments in red, and the length of bifurcation-maximum and bifurcation-bifurcation filaments in grey. The mean length of the maximum-maximum filaments is $6.67\,h^{-1}$ Mpc, comparable to the length of filaments extracted in Rost et al. (2021) from the same gas particle distribution but with different levels of smoothing of the density map and persistence. Due to the exploration of the limited volume of each region, compared to different studies in the literature, the extracted filaments predominantly belong to the short filament population, as has been shown in previous studies (Bond et al. 2010a; Galárraga-Espinosa et al. 2020).

An example of a simulated region at $z = 0$ is shown in Fig. 4a. Here, we display the whole simulated skeleton in grey, while the critical points are represented in the following way: the nodes as red stars, the saddle points as blue dots, and the bifurcation points as yellow triangles. Moreover, we plot the R_{200} spheres of the matched central cluster and less massive groups in the region. A zoom-in of the central cluster and an example of bifurcation points inside the R_{200} sphere are displayed in the bottom panels of the figure, respectively, in Figs. 4a and 4b.

4. Results

To investigate the dependence of cosmic web filaments on the properties of galaxy clusters, we estimated the connectivity of clusters, denoted with k. The connectivity of a galaxy cluster, as it is defined by Codis et al. (2018), is the number of filaments globally connected with the cluster. More specifically, the connectivity is the number of filaments connected to the galaxy cluster at a specific aperture, or in other words, the number of filaments intersecting the surface of a sphere with a certain radius, R_Δ[5].

For the complete dataset, we estimated the connectivity of groups and clusters at R_{500}, R_{200}, and R_{vir}, denoted, respectively,

---

[5] The subscript Δ represents the overdensity, i.e. value of the ratio between the density of the cluster inside that radius and the critical density of the Universe $\rho_c = 3H^2/(8\pi G)$ at the cluster's redshift.
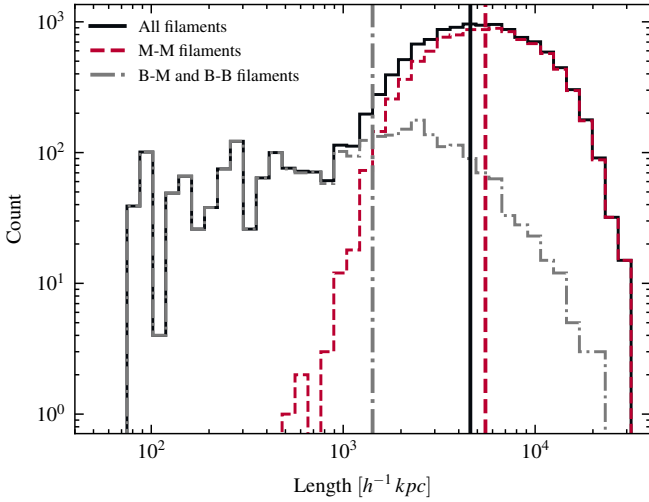
Fig. 3. Filaments length distribution. With the solid black line we plot the distribution of length for the whole sample of filaments, with the dashed red line the length distribution of the filaments with two maxima at the extremes, and with the dash-dotted grey line the length of bifurcation-maximum and bifurcation-bifurcation filaments. The vertical lines are the median values of each distribution.

as k_{500}, k_{200}, and k_{vir}, where the subscript *vir* refers to the virial radius[6]. With this definition, the connectivity value takes into account filaments that start from a node or a bifurcation point within the aperture considered. An example of this phenomenon is displayed in the bottom right panel of Fig. 4c, where the cluster has a connectivity, k_{200}, equal to 7, considering the filaments originating from the bifurcation points inside R_{200}. We observe that, for the sake of redundancy, we omit from the connectivity symbol the subscripts denoting the cosmic web tracer and dimensionality, which in our case should be gas and 3D, although these aspects should always be specified when considering the cosmic web identification.

4.1. Connectivity and galaxy cluster mass

The number of filaments connected to a galaxy cluster – the connectivity – is expected to scale with the cluster's mass. As filaments feed the cluster centre with DM, gas, and galaxies, more connected clusters are on average more massive.

In THE THREE HUNDRED dataset, we estimated the connectivity for 3412 groups and clusters at $z = 0$, with a total mass range of $10^{13} \leq M_{200} \, h^{-1} \, M_\odot \leq 2.62 \times 10^{15}$. Our results of the connectivity as a function of the cluster's mass, M_{200}, at $z = 0$ are presented in Fig. 5. We find the expected correlation between mass and k at all of the apertures explored – R_{500}, R_{200}, and R_{vir} – whose mean values and errors on the mean, computed with the bootstrap method[7], are plotted in red, pink, and blue, respectively. We performed linear fittings, plotted as dashed lines in Fig. 5 and whose parameters are shown in Table 1, as the following: $\log k_\Delta = A \cdot \log M_{200} + B$.

We observe a flattening in the growing trend among low-massive clusters, specifically in the range

---

[6] The virial radius refers to the aperture where the halo satisfies the conditions of the virial theorem.

[7] For the bootstrap re-sampling, we have drawn 1000 new samples with a replacement, i.e. the same data point can be selected several times, each sample with the same length as the original sample. The error is the standard deviation of the new distribution.

$13 \leq \log[M_{200}/h^{-1} \, M_\odot] \leq 14.5$, which is not present for the massive and central clusters. This phenomenon is likely attributed to the intrinsic limitation on the minimum connectivity value, introduced by our sample construction, which cannot be less than one. The clusters for which we computed the connectivity are, in fact, matched with DisPerSE critical nodes, which are, by definition, all linked to at least one filament.

A direct computational consequence of including other critical points, besides the node matched with the cluster, inside the aperture in the estimate of the connectivity is that the connectivity depends on the aperture chosen, with k_{vir} always equal to or larger than k_{200} and k_{500}. This result is also visible in Fig. 5. We note that this effect is more evident for more massive clusters – the clusters at the centre of the simulated boxes – which lie in a denser environment and can have several substructures, leading to more nodes identified by DisPerSE. Further studies are needed to investigate other physical explanations of this phenomenon, such as the diffusion of filaments inside the apertures considered. This result is consistent at larger redshifts – namely, for $z = 1$ and $z = 2$ – as is shown in Appendix A.

Finally, it is worth noting that the linear fits and the findings shown in Fig. 5 were computed based on a constant mass, M_{200}, for both the dataset at R_{500} and R_{Vir}. This decision was made specifically to emphasise how the connectivity of a fixed cluster mass varies with the aperture. Nevertheless, it is important to mention that the positive correlation between the connectivity and mass would persist even if we were to consider the general relationship between $k_\Delta - M_\Delta$.

Our measurements of the connectivity show a strong agreement with other connectivity values from the literature, over a wider mass range. This result is shown in Fig. 6, where we plot THE THREE HUNDRED data compared to other connectivity samples from the literature, estimated from simulations and observations. The data of Aragón-Calvo et al. (2010b), plotted as blue triangles, were derived from a Λ cold DM N-body simulation, where a multi-scale morphological filter (MMF; Aragón-Calvo et al. 2007) was used to extract cosmological structures such as walls, clusters, and filaments. The values of Gouin et al. (2021) and Galárraga-Espinosa et al. (2024) were estimated from hydrodynamical simulations – the IllustrisTNG and the MilleniumTNG, respectively – and are plotted as grey dots (relaxed groups), crosses (unrelaxed groups), and pink triangles. The connectivity value of the simulated Coma cluster of Malavasi et al. (2023), plotted as a violet diamond, was estimated from a DM-only N-body simulation. The observed samples are the AMASCFI cluster sample, plotted as green stars, extracted from the CFHTLS photometric redshift survey of Sarron et al. (2019), and the COSMOS2015 photometric redshift catalogue of Darragh Ford et al. (2019), plotted as yellow squares. The observed connectivity value of the Coma cluster in Malavasi et al. (2020b) was computed from the cosmic web extracted from the Main Galaxy Sample of the Sloan Digital Sky Survey (SDSS) (Malavasi et al. 2020a) and plotted as a red diamond. Lastly, plotted as a brown star and square, respectively, are the 3D and 2D connectivity values of cluster Abell 2744 (Gallo et al. 2024), computed from the spectroscopic galaxy catalogue of Owers et al. (2011) and X-ray data observed by *XMM-Newton* X-ray Observatory (Eckert et al. 2015; Jauzac et al. 2016).

Although the connectivity values span almost the same ranges, it is important to note the differences in how measurements were taken. This difference may include variations in how the connectivity is defined and at which aperture it is estimated,
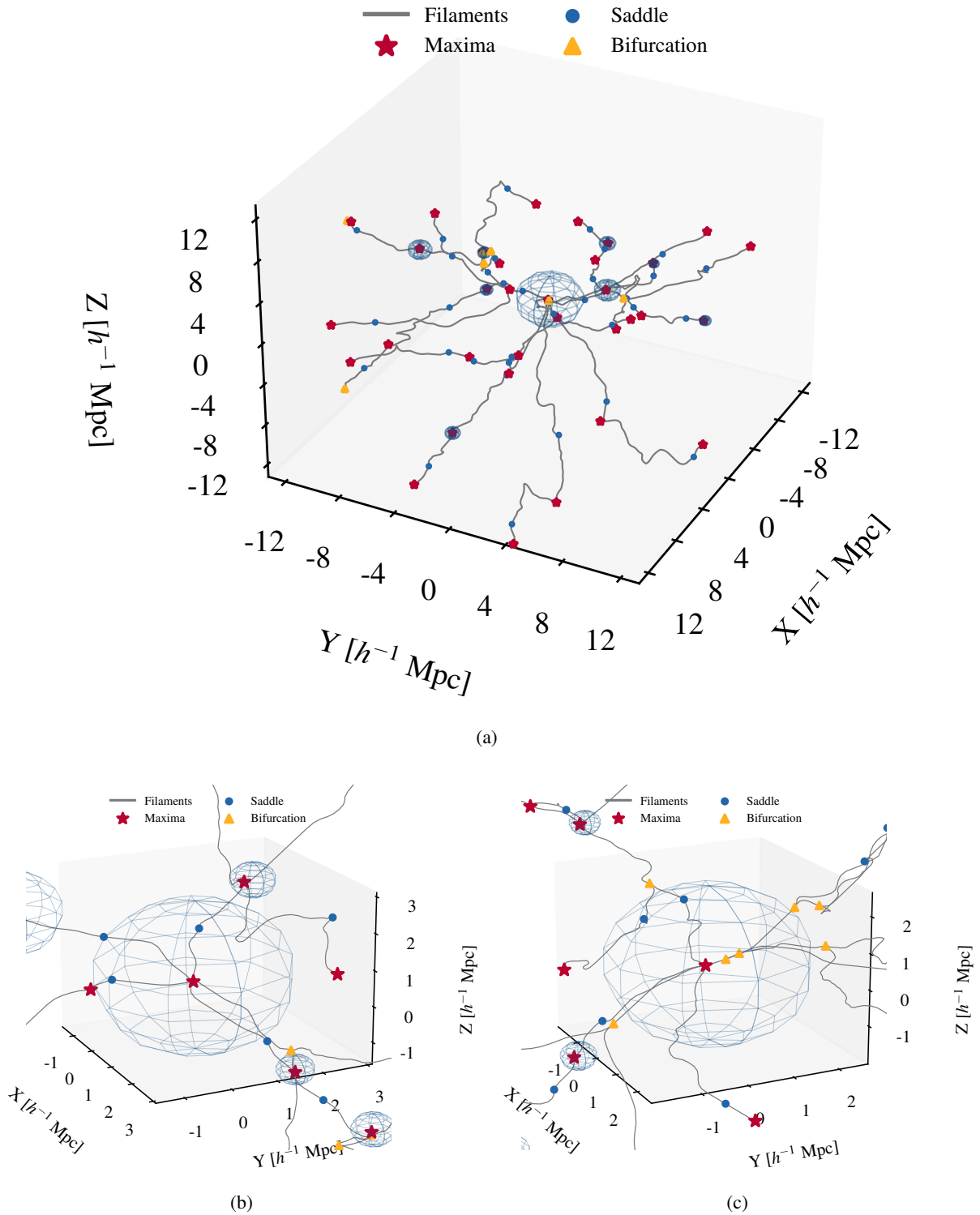
(a)

(b)

(c)

Fig. 4. Examples of DisPerSE simulated networks. Panel (a): Filaments in region 1 at $z = 0$. The full filament network is shown in grey. The nodes are shown as red stars, the saddle points as blue dots, and the bifurcation points as yellow triangles. The light blue spheres are the R_{200} of matched clusters. Panel (b): Zoomed-in view of the central cluster of region 6. Panel (c): Example of two bifurcation points inside the R_{200} sphere of the central cluster of region 2.

the type of tracers used to extract the cosmic web, and the filament finder employed.

Aperture. The connectivity can be computed at a fixed aperture for all the clusters, as in Aragón-Calvo et al. (2010b), where they adopt a fixed aperture of $3\,h^{-1}$ Mpc, and in Sarron et al.

(2019), with a fixed aperture of 1.5 cMpc, or it can be estimated at a set overdensity, as in the case of Darragh Ford et al. (2019), Malavasi et al. (2020b, 2023) and Gallo et al. (2024), whose connectivity is at $1.5\,R_{\rm vir}$, or as Gouin et al. (2021) and Galárraga-Espinosa et al. (2024), with an aperture of $1.5\,R_{200}$.
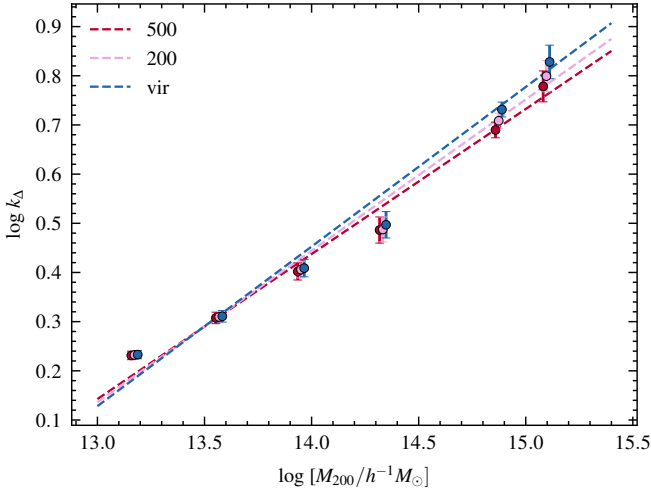
Fig. 5. Mean connectivity of THE THREE HUNDRED groups and clusters at $z = 0$ as a function of the mass, M_{200}. The connectivity was estimated at different over-densities: respectively, k_{500} in red, k_{200} in pink, and k_{vir} in blue. The dashed lines represent the linear fittings. The error bars are the errors on the mean values, computed with the bootstrap method, multiplied by two for visual clarity. The mean values have been shifted in mass for visual clarity.

Table 1. Fitting parameters for the $\log k_\Delta - \log M_{200}$ relation.

Aperture	A	B
R_{500}	0.295 ± 0.016	-3.69 ± 0.24
R_{200}	0.308 ± 0.019	-3.86 ± 0.27
R_{vir}	0.324 ± 0.021	-4.09 ± 0.30

Web finder. The different web finder employed can also affect the recovery of the filamentary structures – and therefore the estimate of the connectivity – since they rely upon different approaches (we refer the reader to Libeskind et al. 2018 for a review of the most common web finders). The most used filament finder is DisPerSE, employed in this work as well as in Sarron et al. (2019), Darragh Ford et al. (2019), Malavasi et al. (2020b, 2023) and Galárraga-Espinosa et al. (2024), although with different parameters tuning. The cosmic web in Gouin et al. (2021) and Gallo et al. (2024) was extracted with the graph-based algorithm T-ReX (Bonnaire et al. 2020).

Cosmic web tracer. In this work, the filamentary structures are traced by the gas particle distribution, in Aragón-Calvo et al. (2007) by DM particles, by X-ray data in the 2D analysis of Gallo et al. (2024), while the remaining studies make use of observed or simulated galaxy catalogues.

Lastly, we note that filaments' identification from 2D tracers can lead to an underestimation of connectivity values, as filaments along the line of sight are often only visible with 3D tracers. This effect is evident in the analysis of Gallo et al. (2024), where the 2D connectivity value of cluster A2744 is smaller than the 3D estimate, due to two filaments along the line of sight being identified only in the 3D analysis using a spectroscopic galaxy catalogue. It is worth noting that the connectivity values of A2744, although they are not directly comparable because of its larger mass, are still lower than those expected from the other analyses presented in Fig. 6. The smaller region analysed for the filament identification (~4 Mpc radius for the 3D analysis and
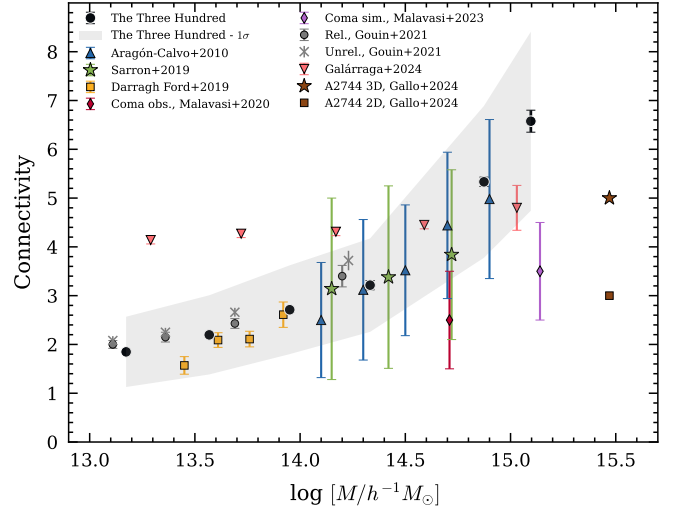

Fig. 6. Connectivity of THE THREE HUNDRED clusters compared to literature values (see the legend for details). The black dots are the mean connectivity values, k_{200}, of THE THREE HUNDRED groups and clusters. The error bars of THE THREE HUNDRED points are the errors on the mean, estimated with the bootstrap method, while the shaded grey area is the standard deviation error. For the literature values, the error bars represent the error on the mean, except for the dataset of Aragón-Calvo et al. (2010b), Sarron et al. (2019), Malavasi et al. (2020b) and Malavasi et al. (2023). For details and differences of each sample, see the main text and Table 2.

~3 Mpc radius for the 2D one) and the sparse galaxy catalogue (305 galaxies) could be the causes of, this difference.

The large difference between the trend followed by THE THREE HUNDRED points and the measurements by Galárraga-Espinosa et al. (2024) at masses lower than $10^{14} h^{-1} M_\odot$ may be related to different choices of the persistence threshold. In general, lower persistence values are needed to connect the extensive sample of clusters of Galárraga-Espinosa et al. (2024), which spans a mass range from 10^{11} to $10^{15} h^{-1} M_\odot$, not entirely shown in Fig. 6. Lower persistence values yield higher numbers of filaments, including weaker and smaller structures, increasing the connectivity measure. A second possible explanation for this difference is suggested in Boldrini & Laigle (2024). They show that a similar trend to the one of Galárraga-Espinosa et al. (2024) emerges when the analysis solely includes groups and clusters with a minimum connectivity of 2. When imposing the same threshold in connectivity – excluding from the analysis the groups with k = 1 – we do observe a small increase in the average connectivity measurements of groups less massive than $10^{14} h^{-1} M_\odot$, although this is still insufficient to match the values of Galárraga-Espinosa et al. (2024).

We did not include in our study, or in Fig. 6, the data published in Einasto et al. (2021) and Aghanim et al. (2024) of clusters in the Corona Borealis supercluster and the Shapley supercluster, respectively. These clusters do not occupy the same parameter space as THE THREE HUNDRED clusters and are not directly comparable, as their connectivity measurement may be biased by the dense environment in which they reside. A future investigation into the connectivity and mass relation for clusters within superclusters could be crucial for understanding the impact of a cluster's environment on its connectivity measurement.

Table 2. Parameters of previous literature studies compared to this work.

Sample	Data	k_R	Mass	CW extraction	Web finder	References
The300	Hydro-sim	R_{200}	M_{200}	3D gas particles	DisPerSE	this work
N-body sim	DM-sim	$3\,h^{-1}$ Mpc	$M_{\rm vir}$	3D DM particles	MMF	1
AMASCFI	Observations	$1.5\,h^{-1}$ Mpc	M_{200}	2D galaxies	DisPerSE	2
COSMOS2015	Observations	$1.5\,R_{\rm vir}$	M_{200}	2D galaxies	DisPerSE	3
Coma obs.	Observations	$1.5\,R_{\rm vir}$	M_{200}	3D galaxies	DisPerSE	4,5
Coma sim.	DM-sim	$1.5\,R_{\rm vir}$	M_{200}	2D galaxies	DisPerSE	6
IllustrisTNG	Hydro-sim	$1.5\,R_{200}$	M_{200}	3D galaxies	T-ReX	7
MilleniumTNG	Hydro-sim	$1.5\,R_{200}$	M_{200}	3D galaxies	DisPerSE	8
Abell 2744 (3D)	Observations	$1.5\,R_{\rm vir}$	M_{200}	3D galaxies	T-Rex	9
Abell 2744 (2D)	Observations	$1.5\,R_{\rm vir}$	M_{200}	X-ray map	T-Rex	9

Notes. (1) Aragón-Calvo et al. (2010b); (2) Sarron et al. (2019); (3) Darragh Ford et al. (2019); (4) Malavasi et al. (2020b) (5) Malavasi et al. (2020a); (6) Malavasi et al. (2023); (7) Gouin et al. (2021); (8) Galárraga-Espinosa et al. (2024); (9) Gallo et al. (2024).

All the studies presented in Fig. 6 confirm a positive correlation between the number of filaments connected to a cluster and its mass, affirming the significant role filaments play in the accretion of matter towards the clusters. However, it is important to take the possible biases into account, summarised in Table 2, when referring to the connectivity.

4.2. Connectivity evolution with redshift

According to the standard theory of anisotropic collapse (Zel'dovich 1970), matter in the Universe is predicted to flow from less dense to denser regions over cosmic time, progressing from walls to filaments and eventually to clusters. As a consequence, in recent times the Universe has predominantly been composed of large under-dense regions – voids – in terms of volume, while clusters and filaments dominate in terms of mass. Moreover, it has been shown (see e.g. Cautun et al. (2014)) that, at high redshift, the filaments of the cosmic web are dominated by thin structures, which are then overtaken by more significant ones at later times. In this framework, we investigated the evolution of cluster connectivity with redshift, which is expected to decrease with cosmic time, as is shown in Codis et al. (2018) and Galárraga-Espinosa et al. (2024).

To detect the cosmic web skeletons at higher redshifts, we created the density maps from the gas particle distributions at redshifts $z = 1.03$ and $z = 2.02$, with the same parameters used for the $z = 0$ sample, with a pixel resolution of $150\,h^{-1}$ kpc and a Gaussian smoothing with an FWHM of 4 pixels. We used the same DisPerSE functions and persistence cut of 0.5, in order to extract filamentary structures with the same robustness and significance. The two final samples have a completeness value of 82% and 83%, respectively, at redshifts $z = 1$ and $z = 2$, indicating that almost every cluster is matched by a node, similar to the sample at $z = 0$.

We compared the connectivity mean values estimated at R_{200} of clusters in the mass range of $10^{13} \leq M_{200}\,h^{-1}\,M_\odot \leq 10^{14}$, populated at all the redshifts explored. In Fig. 7, we plot the connectivity values at $z = 0$ in red, $z = 1$ in purple, and $z = 2$ in yellow. We recovered the expected trend of the connectivity decrease from high redshift to present times, in agreement with what has been found both in theoretical predictions from 2D and 3D estimates (Codis et al. 2018) and, more recently, in hydrodynamical simulations (Galárraga-Espinosa et al. 2024), although with different connectivity values, probably for a similar reason to the one discussed in Sect. 4.1. We observe that for masses below
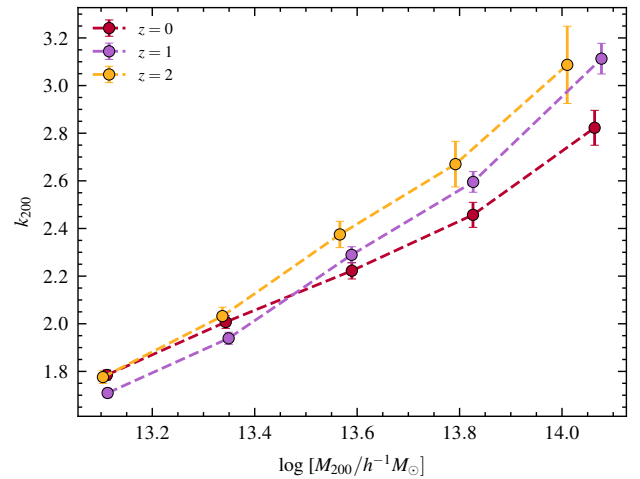

Fig. 7. Evolution with redshift of the connectivity-mass relation. In yellow are shown the mean values of connectivity. k_{200}, extracted from the gas skeleton at $z = 2$, in purple the values at $z = 1$, and in red the values at $z = 0$. The error bars represent the errors on the mean, computed with the bootstrap method.

$2.5 \times 10^{13}\,h^{-1}\,M_\odot$, the connectivity at $z = 0$ shows a flattening trend and remains comparable to the values of higher redshifts. A possible reason for this behaviour can be found in the intrinsic minimum connectivity value introduced by the sample construction, as is explained in detail in Sect. 4.1.

The decrease of connectivity with cosmic time is both a consequence of the anisotropic collapse of the cosmic web structures, with two filaments that merge into one, or a result of their stretch and disconnection caused by the cosmological expansion of void regions in later times due to dark energy. However, further research is required to explore the influence of matter inflow from walls to filaments on filamentary evolution with cosmic time. We note that future studies of the evolution of connectivity with redshift with different dark energy models (see e.g. Codis et al. 2018), and critical events, such as filaments mergers (see e.g. Cadiou et al. 2020), could offer an interesting probe for dark energy models.

4.3. Connectivity and galaxy cluster dynamical state

To investigate if the filaments are related to the dynamical state of galaxy clusters or if the connectivity can be used as a tracer of

the dynamical state, we studied the correlation between the connectivity and the dynamical state of each cluster. In this work, we assess the dynamical state of a cluster following the definition of De Luca et al. (2021), based on 3D dynamical parameters estimated from the physical properties of each particle in the simulation. To evaluate the dynamical state in regions different from the virial radius volumes, we considered two indicators of the cluster's dynamical state, the total sub-halo mass fraction, f_s, and the centre-of-mass offset, Δ_r. The total sub-halo mass fraction, f_s, was defined as the sum of all the sub-halo masses, M_i, identified by AHF within a specific aperture, R_Δ, normalised by the total cluster mass, M_Δ:

$$f_s = \frac{\sum_i M_i}{M_\Delta}. \tag{1}$$

The centre-of-mass offset, Δ_r, was defined as

$$\Delta_r = \frac{|\boldsymbol{r}_{cm} - \boldsymbol{r}_c|}{R_\Delta}, \tag{2}$$

where $\boldsymbol{r}_{cm}$ is the position of the centre-of-mass and $\boldsymbol{r}_c$ is the theoretical centre of the cluster, defined as the highest density peak, which typically coincides with the brightest cluster galaxy. The Δ_r parameter is used to describe the cluster's deviation from smoothness and spherical symmetry, as objects with high values of Δ_r are considered morphologically disturbed.

Specifically, we have classified the clusters as 'relaxed' if both the conditions $f_s < 0.1$ and $\Delta_r < 0.1$ are simultaneously satisfied. On the other hand, a cluster is classified as dynamically 'disturbed' if both $f_s > 0.1$ and $\Delta_r > 0.1$ are true. The clusters whose indicators are not simultaneously verified – therefore, if $f_s > 0.1$ and $\Delta_r < 0.1$ or if $f_s < 0.1$ and $\Delta_r > 0.1$ – are classified as 'hybrid'. In our sample at redshift $z = 0$, 66% of the clusters are classified as relaxed, 20% as hybrid, and 14% as disturbed.

In Fig. 8, we plot the connectivity-mass relation, computed at R_{200}, for the three sub-samples of dynamical state; respectively, relaxed clusters in green, hybrid ones in yellow, and unrelaxed ones in light blue. The three sub-samples overlap and are comparable to each other, within the errors estimated with the bootstrap method, indicating that the connectivity-mass relation is not affected by the dynamical state – assessed in terms of the two indicators, f_s and Δ_r – of the cluster. This result is not dependent on the redshift, as is shown in Appendix B, where we present this analysis at redshifts $z = 1$ and 2, or on the overdensity at which the connectivity and the dynamical state are estimated, as is shown in Appendix C, where we present the same analysis for R_{500} and R_{vir}.

To further investigate the relation between the dynamical state of the cluster and the filaments connected to it, we now focus on the continuous dynamical state indicator, χ. The degree of relaxation combines the dynamical parameters in a single measure of the cluster dynamical state and is defined by Haggar et al. (2020) as

$$\chi = \left[\frac{\sum_i (\frac{x_i}{x_{0,i}})^2}{N} \right]^{-1/2}, \tag{3}$$

where x_i is the general indicator of the dynamical state, $x_{0,i}$ is the threshold between the relaxed and the disturbed regimes, and N is the number of indicators used. As a result, larger values of χ (with $\log \chi > 0$) indicate a more relaxed dynamical state, while negative values of $\log \chi$ represent a disturbed dynamical state. In the literature, the definition of the degree of relaxation can vary both in the choice of the parameters used and in the
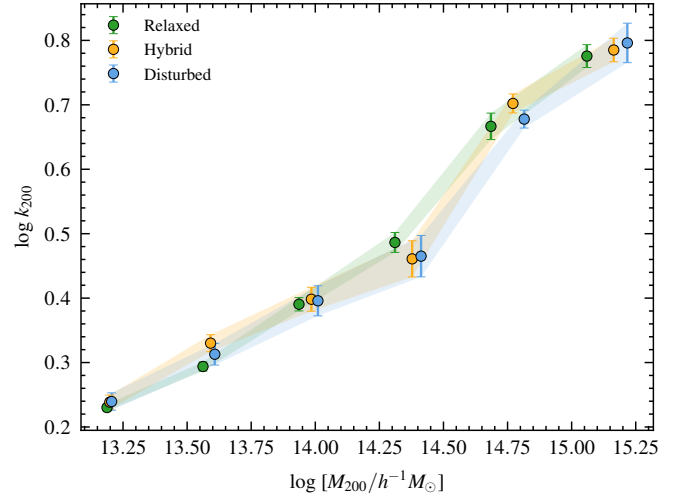

Fig. 8. Connectivity and mass relation for three dynamical state subsamples at redshift $z = 0$. In green are shown the connectivity mean values, k_{200}, for the dynamically relaxed clusters, in yellow the values for hybrid clusters, and in light blue the ones for dynamically disturbed clusters. The error bars represent the errors of the mean, computed with the bootstrap method.

selection of the threshold values (see e.g. Cui et al. 2017). In this work, we estimated χ with f_s and Δ_r, both considered with a threshold of 0.1. We estimated the dynamical state of the clusters at redshift $z = 0$ and computed the degree of relaxation as in Eq. (3), considering the parameters at R_{200}.

To possibly disentangle the impact of connectivity and mass on the dynamical state, given their correlation, we divided the total dataset into three bins of connectivity and three bins of mass. This approach is necessary to study the relationship between the degree of relaxation and the connectivity independently of the mass, and vice versa.

The three connectivity bins divide the dataset into ~700 weakly connected groups with $k_{200} < 2$, ~2000 average-connected clusters with $k_{200} \in \{2, 3\}$, and ~500 highly connected clusters with $k_{200} > 3$. These thresholds were chosen taking the mean connectivity value of $k_{200} = 2.42$ of the whole cluster population at redshift $z = 0$ into account.

In the left panel (a) of Fig. 9, we plot the mean degree of relaxation as a function of mass for the three connectivity subsamples; respectively, in green the weakly connected clusters, in yellow the average-connected ones, and in light blue the highly connected ones. At fixed mass, the three connectivity bins overlap and are comparable to each other within the errors, confirming that the connectivity does not influence the dynamical state of the cluster, computed with the f_s and Δ_r, corroborating the result shown in Fig. 8.

This outcome is not consistent with that of Gouin et al. (2021) who found a correlation between the degree of relaxation and the connectivity values, with more connected clusters being on average more dynamically unrelaxed. We note that the disagreement could be due to the different definition of the degree of relaxation used in Gouin et al. (2021), which differs from ours in the dynamical indicators and thresholds used, as well as the differences in the dataset and the cosmic web extraction, as is illustrated in Table 2.

Focusing now on the mass bins, we divided the dataset into low-mass groups with $M_{200} < 5 \times 10^{13} \, h^{-1} \, M_\odot$, medium groups and clusters with $5 \times 10^{13} \le M_{200} \, h^{-1} \, M_\odot < 5.5 \times 10^{14}$, and massive clusters with $M_{200} \ge 5.5 \times 10^{14} \, h^{-1} \, M_\odot$, which

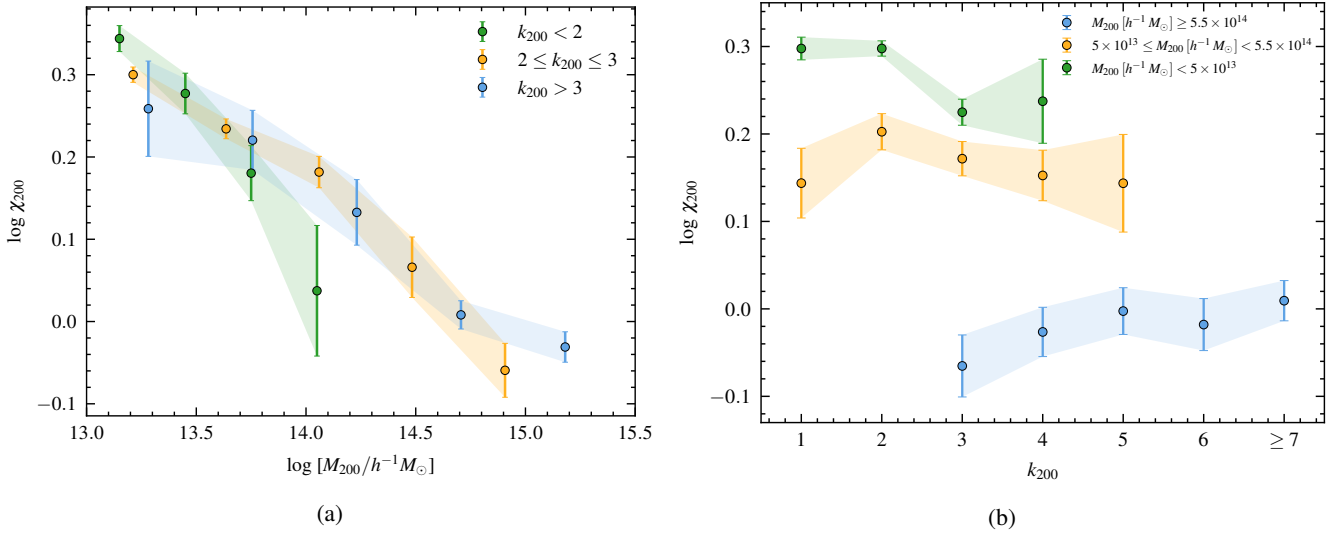(a)   (b)

Fig. 9. Dynamical state dependence on connectivity and cluster total mass at redshift $z = 0$. Panel (a): Degree of relaxation, χ_{200}, as a function of the total mass, M_{200}. Green, yellow, and light blue dots indicate, respectively, weakly connected ($k_{200} < 2$), average-connected ($k_{200} \in \{2, 3\}$), and highly connected ($k_{200} > 3$) clusters. Panel (b): Degree of relaxation, χ_{200}, as a function of the connectivity, k_{200}. Green, yellow, and light blue dots indicate, respectively, low-mass ($M_{200} < 5 \times 10^{13} \, h^{-1} \, M_\odot$), medium ($5 \times 10^{13} \leq M_{200} \, h^{-1} \, M_\odot < 5.5 \times 10^{14}$), and massive ($M_{200} \geq 5.5 \times 10^{14} \, h^{-1} \, M_\odot$) clusters. The shaded areas and the error bars indicate the error of the mean, computed with the bootstrap method.

correspond to the large galaxy clusters at the centre of each simulated region. The three sub-samples are plotted in the right panel (b) of Fig. 9 in green, yellow, and light blue, respectively. Contrary to the connectivity sub-samples shown in Fig. 9a, at fixed connectivity the three mass bins show a distinct separation from one another. This behaviour suggests a correlation between the degree of relaxation, χ_{200}, and the mass of the cluster, independently of their connectivity value, with less massive groups appearing to be more dynamically relaxed, and vice versa.

This result was also reported by Kuchner et al. (2020) – although with a different definition of the degree of relaxation, both in the parameters and the thresholds chosen – who suggest that the most massive clusters tend to be in a more dynamically disturbed state. This phenomenon is likely attributed to the fact that the most massive clusters are currently still growing, resulting in larger centre-of-mass offsets and in the presence of internal substructures (Power et al. 2012). Moreover, the high-density environment in which they are situated can make them more likely to accrete matter, resulting in less relaxed states (Kuchner et al. 2020).

4.4. Connectivity and mass bias

Classical approaches to inferring the mass of galaxy clusters from SZ and X-rays observations usually rely on the hydrostatic equilibrium (HE) assumption (for a review, see Kravtsov & Borgani 2012). This hypothesis assumes that the gas thermal pressure is balanced by the gravitational forces, leading the cluster to a state of equilibrium. Deviations from the HE can introduce errors in the estimation of observable properties of clusters and their mass.

We investigated if the presence of filaments, quantified with the connectivity, has an impact on the HE of the galaxy clusters of THE THREE HUNDRED simulation. For this purpose, we refer to the analysis of Gianfagna et al. (2023), who explored the deviations of the HE mass, M_{HE}, from the total mass M_{true} of the 324 simulated central clusters, quantified with the hydrostatic mass bias, b. M_{true} refers to the real mass, computed by summing all

the DM, gas, and star particle masses inside a radius. On the other hand, the HE mass, M_{HE}, is the mass inferred from the gas thermal pressure profile estimated from SZ observations or from the temperature and electron density profiles from X-ray observations, leading, respectively, to the mass biases b_{SZ} and b_X, defined as:

$$b = \frac{M_{\text{true}} - M_{HE}}{M_{\text{true}}}. \qquad (4)$$

We refer to Gianfagna et al. (2023) for the complete derivation of the parameters. We note that a positive bias, if defined in this way, denotes an underestimation of the true mass.

We plot in Fig. 10 the median values of the hydrostatic mass biases, b_{SZ} and b_X, estimated at R_{200} as a function of the connectivity, k_{200}, of the cluster. No correlation is found between the bias and the connectivity, independently of the observable property used to estimate it. Moreover, we note that we do not observe any variation in the scatter with connectivity, meaning that the dispersion of the bias is independent of the number of filaments connected. On the other hand, the scatter of the hydrostatic mass bias has been found to vary as a function of the dynamical state, quantified with different indicators, with disturbed clusters showing a wider dispersion (Piffaretti & Valdarnini 2008; Rasia et al. 2012; Ansarifard et al. 2020; Gianfagna et al. 2023). This result suggests that the connectivity may not be used as a reliable indicator of the dynamical state of a galaxy cluster, as was already shown in Sect. 4.3. The same result is observed for the connectivity and the bias estimated at R_{500}, as is shown in Appendix D.

5. Mock-galaxy filaments

In this section, we aim to investigate the effect of the chosen tracer on the extraction of the cosmic web. In this context, we compare the connectivity estimates from filaments extracted from the gas particle distribution to those identified from the mock-galaxy distribution in THE THREE HUNDRED regions.
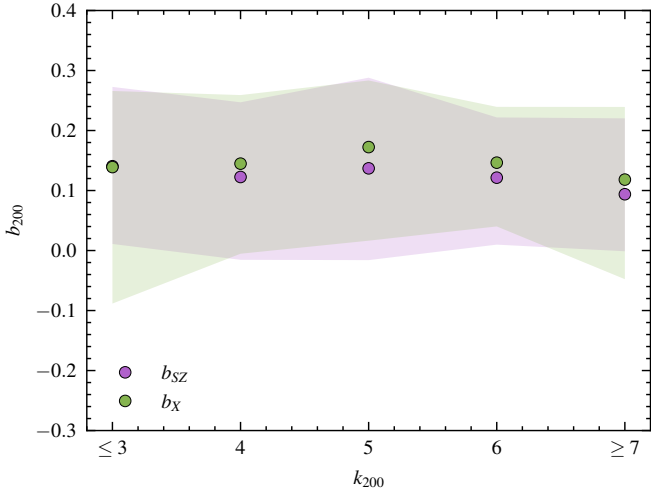
Fig. 10. Connectivity and hydrostatic mass bias relation at redshift $z = 0$. In green are shown the mass bias median values, b_X, at R_{200} and in violet the mass bias median values, b_{SZ}, at R_{200}. The shaded areas represent the 16th and 84th percentiles.

Fig. 11. Mean connectivity of The Three Hundred groups and clusters at $z = 0$, estimated from gas and mock-galaxy filaments. The mean values of connectivity, k_{200}, from gas filaments are plotted in blue, and the values of k_{200} from mock-galaxy filaments are plotted in red. The solid and dashed lines represent the linear fitting for the gas and the mock galaxies, respectively. The error bars are the errors on the mean values, computed with the bootstrap method.

Table 3. Fitting parameters for the $\log k_{200} - \log M_{200}$ relation for gas-traced filaments and mock-galaxy-traced filaments.

Tracer	A	B
Mock-galaxies	0.291 ± 0.018	-3.66 ± 0.26
Gas	0.308 ± 0.019	-3.86 ± 0.27

The simulated cosmic web is traced by the mock galaxy catalogue of the full $1\,h^{-1}$ Gpc MDPL2 box at redshift $z = 0$. Haloes are defined as a mock galaxy if they have a minimum stellar mass of $M_* \geq 3 \times 10^9\,h^{-1}\,M_\odot$, which corresponds to haloes with $M_{\mathrm{halo}} > 3 \times 10^{10}\,h^{-1}\,M_\odot$. The density is computed from the Delaunay tessellation of the points with the DTFE. The tessellation is mass-weighted, with a weight associated with each tessellation vertex corresponding to the mass of the halo at this vertex, to improve the filament identification, as is explained in detail by Kuchner et al. (2020). The cosmic web skeleton is then identified with DisPerSE with a persistence ratio threshold of 6.5σ, which provides the best agreement with the cosmic web extracted from gas particles, as is tested in Kuchner et al. (2020). A more detailed description of the extraction procedure and in-depth analysis of filament properties from the full MDPL2 box will be provided in a dedicated paper (Bianconi et al., in prep.).

We associated the DisPerSE nodes with simulated groups, considering as matched those with a distance of less than 4 pixels, as is explained in detail in Sect. 3.2. The final sample, for all the 324 regions, includes 836 galaxy groups and clusters with a mass range of $10^{13} \leq M_{200}\,h^{-1}\,M_\odot \leq 2.69 \times 10^{15}$. Lastly, we estimated the connectivity, k_{200}, of the galaxy clusters at R_{200}, as is defined in Sect. 4.

The results of the connectivity, k_{200}, estimated from mock-galaxy filaments are plotted in Fig. 11 in red, as a function of the cluster's mass, M_{200}. We plot as blue dots the connectivity values computed from gas filaments, presented in Sect. 4.1. We performed the same linear fitting as for the gas connectivity, whose parameters are shown in Table 3.

The strong agreement between the two connectivities is an indication that the number of filaments traced by gas or mock galaxies is similar, and therefore that these are representative of the same structures. A similar result in The Three Hundred simulation was shown in Kuchner et al. (2020), where they measure the distance between gas-traced and galaxy-traced filaments. They find a median value of $0.67\,h^{-1}$ Mpc for the distribution of distance between the two skeletons. This value lowers to $0.47\,h^{-1}$ Mpc when taking only mass-weighted galaxies into account, as in the case of our work. Both values are lower than the typical thickness of a filament. However, potential
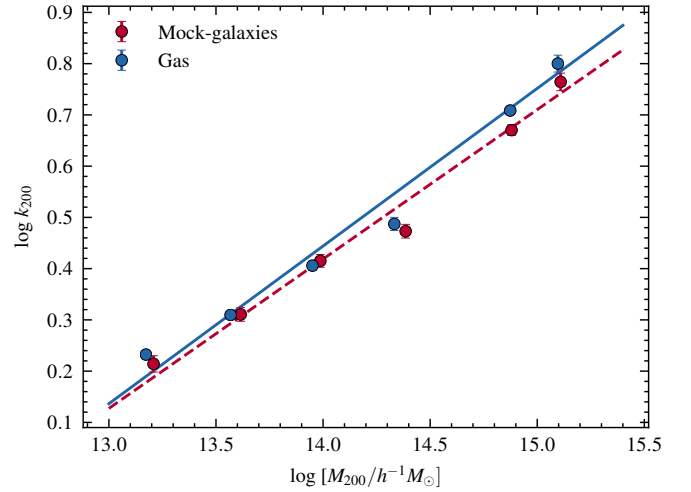
discrepancies between the skeletons extracted from gas or DM particles and haloes catalogues are expected, as has been noted in other studies (e.g. Bond et al. 2010a,b; Laigle et al. 2018; Kuchner et al. 2020; Zakharova et al. 2023). These discrepancies are likely to be attributed to the finer sampling of the density field by gas particles, which outnumber the mock galaxies, and therefore could result in reduced noise during the cosmic web extraction process. Moreover, employing different density field estimation methods – a regular grid for the gas particles and the Delaunay tessellation for the mock galaxies – may introduce some variations in the extracted skeletons, such as a preferred direction for the filamentary structures. The discrepancies between the two tracers and the effects on the recovered cosmic web are investigated more in detail by Bianconi et al. (in prep.).

6. Conclusions

The outskirts of galaxy clusters can provide insightful information for the study of large-scale structures. In particular, the presence of filamentary structures, acting as pathways for matter transportation towards the centre of clusters, and their impact on clusters' properties can be investigated. The aim of this study is to examine the correlation between the connectivity and the main galaxy clusters properties.

In this work, we have used the 324 regions with a $30\,h^{-1}$ Mpc side of The Three Hundred hydrodynamical simulation to extract the filamentary structures around galaxy clusters and groups. We ran the DisPerSE algorithm on the gas particle density maps at redshifts $z = 0, 1$, and 2. The full procedure of

generating the density maps has been described, together with the setting of relevant parameters of DisPerSE. We have estimated the connectivity at several apertures, in particular at R_{500}, R_{200}, and R_{vir} for $\sim 10^3$ groups and clusters with a total mass range of $10^{13} \leq M_{200}\,h^{-1}\,M_\odot \leq 2.62 \times 10^{15}$ at redshift $z = 0$.

The main results of this work can be summarised as follows:

(i) The connectivity, computed as the number of gas filaments crossing the sphere at a specific aperture, quantified in terms of overdensity, depends on the chosen radius, with larger values of connectivity when estimated at larger radii. This is a consequence of including filaments that start from substructures – maxima and bifurcation points – that lie within the radius considered. Therefore, it is important to specify the aperture chosen when analysing the connectivity of galaxy clusters.

(ii) Filaments have an impact on galaxy cluster mass accretion, transporting matter from the outskirts to the centre. On average, more massive galaxy clusters are also more connected. This result is in agreement with several literature studies, both from observed and simulated datasets.

(iii) We observe a decrease in the connectivity mean values over cosmic time, with clusters being more connected at higher redshifts. This result is likely to be a consequence of the anisotropic collapse of the cosmic web structures.

(iv) No dependence of connectivity with the cluster's dynamical state is found. The connectivity-mass correlation does not have any significant difference when computed for three sub-samples of clusters: dynamically relaxed, hybrid, and disturbed. Moreover, we do not observe any correlation between the connectivity and the degree of relaxation parameter, χ. On the other hand, we find that, independently of the connectivity, more massive clusters are on average more dynamically disturbed.

(v) No correlation of the hydrostatic mass bias with redshift is found for the 324 central clusters. This result is independent of the aperture at which the quantities are computed and the observable properties used to infer the hydrostatic mass bias. Moreover, we do not observe a variation in the scatter of the bias with the connectivity, contrary to what is found with the dynamical state of clusters. This suggests that the connectivity may not be an indicator of the dynamical state.

(vi) We observe a strong agreement between the connectivity evaluated from gas-traced filaments and mock-galaxy-traced filaments, extracted from the mock haloes catalogue of the full MDPL2 box. This result suggests that gas and mock galaxies trace a comparable number of structures, yielding a similar connectivity value, and offer similar conclusions on the overall connections of the cosmic web.

This work underlines the dependence of filaments, traced by the gas particle distribution, on the properties of the galaxy clusters to which they are connected and shows a correlation between the connectivity and the total mass of the clusters. This result affirms the role that filaments play in the accretion of matter towards the centre of the cluster.

The results presented in this work and the simulated cosmic web skeletons will be used as a reference for cosmic web extraction from Compton-y simulated maps, to provide insightful forecasts for observations. With further investigations on filaments' evolution with cosmic time, useful information on the study of cosmology and structure evolution can be provided. Further work is needed to assess the differences in the cosmic web extraction process from distinct tracers and from different density field estimation methods. Future analysis with different hydrodynamical codes, such as the GIZMO-SIMBA run of THE

THREE HUNDRED (Cui et al. 2022), will be necessary to investigate the dependence of the results on different baryonic models.

References

Aghanim, N., Tuominen, T., Bonjean, V., et al. 2024, A&A, 689, A332
Alpaslan, M., Robotham, A. S. G., Driver, S., et al. 2014, MNRAS, 438, 177
Ansarifard, S., Rasia, E., Biffi, V., et al. 2020, A&A, 634, A113
Aragón-Calvo, M. A., Jones, B. J. T., van de Weygaert, R., & van der Hulst, J. M. 2007, A&A, 474, 315
Aragón-Calvo, M. A., Platen, E., van de Weygaert, R., & Szalay, A. S. 2010a, ApJ, 723, 364
Aragón-Calvo, M. A., van de Weygaert, R., & Jones, B. J. T. 2010b, MNRAS, 408, 2163
Beck, A. M., Murante, G., Arth, A., et al. 2016, MNRAS, 455, 2110
Boldrini, P., & Laigle, C. 2024, A&A, submitted [arXiv:2402.04837]
Bond, J. R., Kofman, L., & Pogosyan, D. 1996, Nature, 380, 603
Bond, N. A., Strauss, M. A., & Cen, R. 2010a, MNRAS, 406, 1609
Bond, N. A., Strauss, M. A., & Cen, R. 2010b, MNRAS, 409, 156
Bonjean, V., Aghanim, N., Salomé, P., Douspis, M., & Beelen, A. 2018, A&A, 609, A49
Bonnaire, T., Aghanim, N., Decelle, A., & Douspis, M. 2020, A&A, 637, A18
Boselli, A., & Gavazzi, G. 2006, PASP, 118, 517
Boselli, A., & Gavazzi, G. 2014, A&ARv, 22, 74
Bulichi, T.-E., Davé, R., & Kraljic, K. 2024, MNRAS, 529, 2595
Cadiou, C., Pichon, C., Codis, S., et al. 2020, MNRAS, 496, 4787
Cautun, M., van de Weygaert, R., & Jones, B. J. T. 2013, MNRAS, 429, 1286
Cautun, M., van de Weygaert, R., Jones, B. J. T., & Frenk, C. S. 2014, MNRAS, 441, 2923
Codis, S., Pogosyan, D., & Pichon, C. 2018, MNRAS, 479, 973
Cohn, J. D. 2022, MNRAS, 513, 624
Colless, M., Dalton, G., Maddox, S., et al. 2001, MNRAS, 328, 1039
Cornwell, D. J., Kuchner, U., Gray, M. E., et al. 2024, MNRAS, 527, 23
Cui, W., Power, C., Borgani, S., et al. 2017, MNRAS, 464, 2502
Cui, W., Knebe, A., Yepes, G., et al. 2018a, MNRAS, 480, 2898
Cui, W., Knebe, A., Yepes, G., et al. 2018b, MNRAS, 473, 68
Cui, W., Dave, R., Knebe, A., et al. 2022, MNRAS, 514, 977
Danforth, C. W., Keeney, B. A., Tilton, E. M., et al. 2016, ApJ, 817, 111
Darragh Ford, E., Laigle, C., Gozaliasl, G., et al. 2019, MNRAS, 489, 5695
Davé, R., Cen, R., Ostriker, J. P., et al. 2001, ApJ, 552, 473
Davé, R., Anglés-Alcázar, D., Narayanan, D., et al. 2019, MNRAS, 486, 2827
De Luca, F., De Petris, M., Yepes, G., et al. 2021, MNRAS, 504, 5383
Donnan, C. T., Tojeiro, R., & Kraljic, K. 2022, NatAs, 6, 599
Eckert, D., Jauzac, M., Shan, H., et al. 2015, Nature, 528, 105
Edelsbrunner, H., Letscher, D., & Zomorodian, A. 2002, Discr. Comput. Geometry, 28, 511
Einasto, M., Kipper, R., Tenjes, P., et al. 2021, A&A, 649, A51
Falck, B. L., Neyrinck, M. C., & Szalay, A. S. 2012, ApJ, 754, 126

Forero-Romero, J. E., Hoffman, Y., Gottlöber, S., Klypin, A., & Yepes, G. 2009, MNRAS, 396, 1815
Forman, R. 1998, Adv. Math., 134, 90
Galárraga-Espinosa, D., Aghanim, N., Langer, M., Gouin, C., & Malavasi, N. 2020, A&A, 641, A173
Galárraga-Espinosa, D., Cadiou, C., Gouin, C., et al. 2024, A&A, 684, A63
Gallo, S., Aghanim, N., Gouin, C., et al. 2024, A&A, submitted [arXiv:2407.10518]
Gianfagna, G., Rasia, E., Cui, W., et al. 2023, MNRAS, 518, 4238
Gouin, C., Bonnaire, T., & Aghanim, N. 2021, A&A, 651, A56
Gyulassy, A., Bremer, P.-T., Hamann, B., & Pascucci, V. 2008, IEEE Trans. Visual. Comput. Graphics, 14, 1619
Haggar, R., Gray, M. E., Pearce, F. R., et al. 2020, MNRAS, 492, 6074
Hellwing, W. A., Cautun, M., van de Weygaert, R., & Jones, B. T. 2021, Phys. Rev. D, 103, 063517
Hernández-Aguayo, C., Springel, V., Pakmor, R., et al. 2023, MNRAS, 524, 2556
Hincks, A. D., Radiconi, F., Romero, C., et al. 2022, MNRAS, 510, 3335
Hoffman, Y., Metuki, O., Yepes, G., et al. 2012, MNRAS, 425, 2049
Jauzac, M., Richard, J., Jullo, E., et al. 2016, VizieR On-line Data Catalog: J/MNRAS/452/1437
Klypin, A., Yepes, G., Gottlöber, S., Prada, F., & Heß, S. 2016, MNRAS, 457, 4340
Knollmann, S. R., & Knebe, A. 2011, Astrophysics Source Code Library [record ascl:1102.009]
Kotecha, S., Welker, C., Zhou, Z., et al. 2022, MNRAS, 512, 926
Kraljic, K., Arnouts, S., Pichon, C., et al. 2018, MNRAS, 474, 547
Kravtsov, A. V., & Borgani, S. 2012, ARA&A, 50, 353
Kuchner, U., Aragón-Salamanca, A., Pearce, F. R., et al. 2020, MNRAS, 494, 5473
Kuchner, U., Aragón-Salamanca, A., Rost, A., et al. 2021, MNRAS, 503, 2065
Kuchner, U., Haggar, R., Aragón-Salamanca, A., et al. 2022, MNRAS, 510, 581
Laigle, C., Pichon, C., Arnouts, S., et al. 2018, MNRAS, 474, 5437
Libeskind, N. I., van de Weygaert, R., Cautun, M., et al. 2018, MNRAS, 473, 1195
Lokken, M., Cui, W., Bond, J. R., et al. 2023, MNRAS, 523, 1346
Malavasi, N., Aghanim, N., Douspis, M., Tanimura, H., & Bonjean, V. 2020a, A&A, 642, A19
Malavasi, N., Aghanim, N., Tanimura, H., Bonjean, V., & Douspis, M. 2020b, A&A, 634, A30
Malavasi, N., Langer, M., Aghanim, N., Galárraga-Espinosa, D., & Gouin, C. 2022, A&A, 658, A113
Malavasi, N., Sorce, J. G., Dolag, K., & Aghanim, N. 2023, A&A, 675, A76
Nelson, D., Springel, V., Pillepich, A., et al. 2019, ComAC, 6, 2
Nicastro, F., Kaastra, J., Krongold, Y., et al. 2018, Nature, 558, 406
Owers, M. S., Randall, S. W., Nulsen, P. E. J., et al. 2011, ApJ, 728, 27
Peebles, P. J. E. 1980, The large-scale structure of the universe
Piffaretti, R., & Valdarnini, R. 2008, A&A, 491, 71
Planck Collaboration XIII. 2016, A&A, 594, A13
Power, C., Knebe, A., & Knollmann, S. R. 2012, MNRAS, 419, 1576
Rasia, E., Meneghetti, M., Martino, R., et al. 2012, NJPh, 14, 055018
Rost, A., Kuchner, U., Welker, C., et al. 2021, MNRAS, 502, 714
Rost, A. M., Nuza, S. E., Stasyszyn, F., et al. 2024, MNRAS, 527, 1301
Sarron, F., Adami, C., Durret, F., & Laigle, C. 2019, A&A, 632, A49
Schaap, W. E., & van de Weygaert, R. 2000, A&A, 363, L29
Schaye, J., Crain, R. A., Bower, R. G., et al. 2015, MNRAS, 446, 521
Shull, J. M., Smith, B. D., & Danforth, C. W. 2012, ApJ, 759, 23
Song, H., Laigle, C., Hwang, H. S., et al. 2021, MNRAS, 501, 4635
Sousbie, T. 2011, MNRAS, 414, 350
Sousbie, T., Pichon, C., & Kawahara, H. 2011, MNRAS, 414, 384
Springel, V. 2005, MNRAS, 364, 1105
Springel, V., & Hernquist, L. 2003, MNRAS, 339, 312
Steinborn, L. K., Dolag, K., Hirschmann, M., Prieto, M. A., & Remus, R.-S. 2015, MNRAS, 448, 1504
Tanimura, H., Aghanim, N., Douspis, M., Beelen, A., & Bonjean, V. 2019, A&A, 625, A67
Tanimura, H., Aghanim, N., Kolodzig, A., Douspis, M., & Malavasi, N. 2020, A&A, 643, L2
Tanimura, H., Aghanim, N., Douspis, M., & Malavasi, N. 2022, A&A, 667, A161
Tempel, E., Stoica, R. S., Kipper, R., & Saar, E. 2016, A&C, 16, 17
Tornatore, L., Borgani, S., Dolag, K., & Matteucci, F. 2007, MNRAS, 382, 1050
Tuominen, T., Nevalainen, J., Tempel, E., et al. 2021, A&A, 646, A156
van de Weygaert, R., & Schaap, W. 2009, in The Cosmic Web: Geometric Analysis, eds. V. J. Martinez, E. Saar, E. M. Gonzales, & M. J. Pons-Borderia (Berlin, Heidelberg: Springer), 291
Vogelsberger, M., Genel, S., Springel, V., et al. 2014, Nature, 509, 177
Winkel, N., Pasquali, A., Kraljic, K., et al. 2021, MNRAS, 505, 4920
York, D. G., Adelman, J., Anderson, Jr., J. E., et al. 2000, AJ, 120, 1579
Zakharova, D., Vulcani, B., De Lucia, G., et al. 2023, MNRAS, 525, 4079
Zel'dovich, Y. B. 1970, A&A, 5, 84

Appendix A: Connectivity and cluster overdensity at higher redshifts

The connectivity depends on the aperture at which it is estimated, independently of the redshift. We plot the mean values of k_{500}, k_{200}, and k_{vir} as a function of the cluster mass at redshift $z = 1$ and $z = 2$, respectively in Figs. A.1 and A.2.
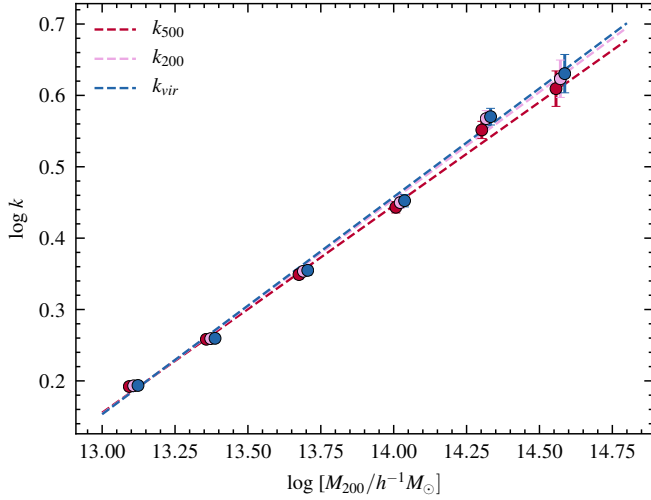

Fig. A.1. Mean connectivity of THE THREE HUNDRED groups and clusters at $z = 1$ as a function of the mass M_{200}. The connectivity was estimated at different over-densities: respectively, k_{500} in red, k_{200} in pink, and k_{vir} in blue. The dashed lines represent the linear fitting. The error bars are the errors on the mean values, computed with the bootstrap method. The mean values have been shifted in mass for visual clarity.
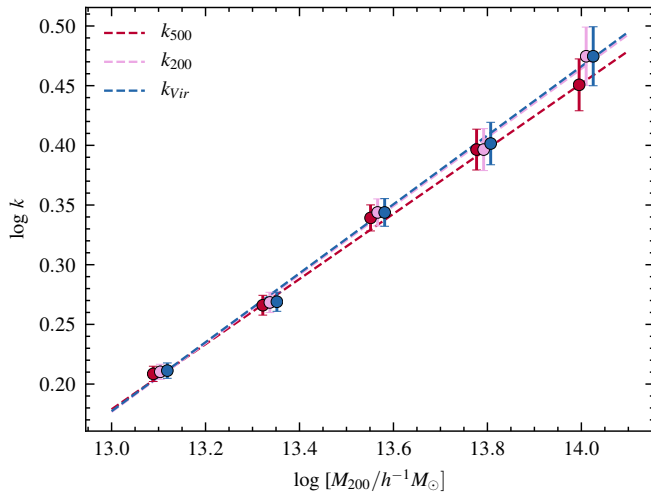

Fig. A.2. Mean connectivity of THE THREE HUNDRED groups and clusters at $z = 2$ as a function of the mass M_{200}. The connectivity was estimated at different over-densities: respectively,k_{500} in red, k_{200} in pink, and k_{vir} in blue. The dashed lines represent the linear fitting. The error bars are the errors on the mean values, computed with the bootstrap method. The mean values have been shifted in mass for visual clarity.

Appendix B: Connectivity and dynamical state at higher redshifts

The connectivity and mass correlation is not dependent on the dynamical state of the cluster, regardless of the redshift. We plot in Figs. B.1 and B.2 the connectivity mean values as a function of the mass for dynamically relaxed, hybrid, and disturbed clusters, respectively at redshift $z = 1$ and $z = 2$.
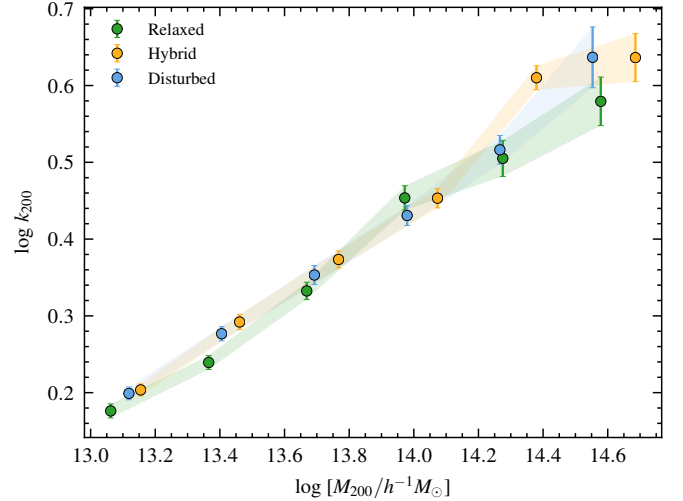

Fig. B.1. Connectivity and mass relation for three dynamical state subsamples at redshift $z = 1$. In green are shown the connectivity mean values, k_{200}, for the dynamically relaxed clusters, in yellow the values for hybrid clusters, and in light blue the ones for dynamically disturbed clusters. The error bars represent the errors of the mean, computed with the bootstrap method.
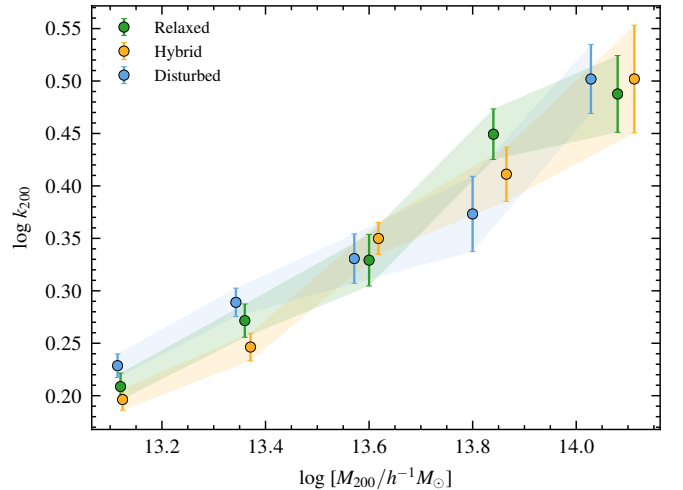

Fig. B.2. Connectivity and mass relation for three dynamical state subsamples at redshift $z = 2$. In green are shown the connectivity mean values, k_{200}, for the dynamically relaxed clusters, in yellow the values for hybrid clusters, and in light blue the ones for dynamically disturbed clusters. The error bars represent the errors of the mean, computed with the bootstrap method.

Appendix C: Connectivity and dynamical state at different overdensities

The connectivity and mass correlation is not dependent on the dynamical state of the cluster, independently of the overdensity at which the connectivity and the dynamical state are estimated. We plot in Figs. C.1 and C.2 the connectivity mean values as a function of the mass for dynamically relaxed, hybrid and disturbed clusters, estimated respectively at R_{500} and R_{vir}.
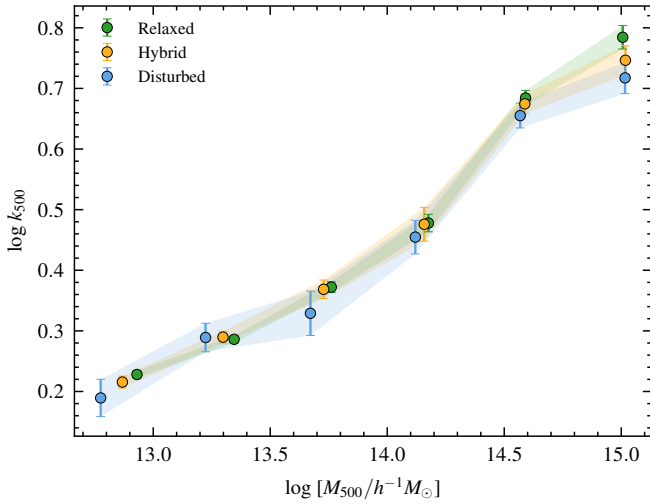

Fig. C.1. Connectivity and mass relation for three dynamical state subsamples at redshift $z = 0$, estimated at R_{500}. In green are shown the connectivity mean values, k_{500}, for the dynamically relaxed clusters, in yellow the values for hybrid clusters, and in light blue the ones for dynamically disturbed clusters. The error bars represent the errors of the mean, computed with the bootstrap method.
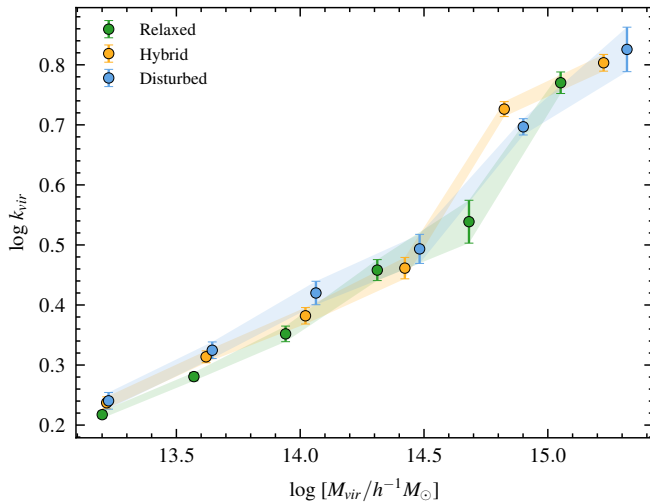

Fig. C.2. Connectivity and mass relation for three dynamical state subsamples at redshift $z = 0$, estimated at R_{vir}. In green are shown the connectivity mean values, k_{vir}, for the dynamically relaxed clusters, in yellow the values for hybrid clusters, and in light blue the ones for dynamically disturbed clusters. The error bars represent the errors of the mean, computed with the bootstrap method.

Appendix D: Connectivity and HE bias at R_{500}

We plot a in Fig. D.1 the median values of the hydrostatic mass biases b_X, in green, and b_{SZ}, in violet, computed at R_{500} as a function of the connectivity k_{500}. A correlation between the connectivity and the hydrostatic mass bias is not observed.
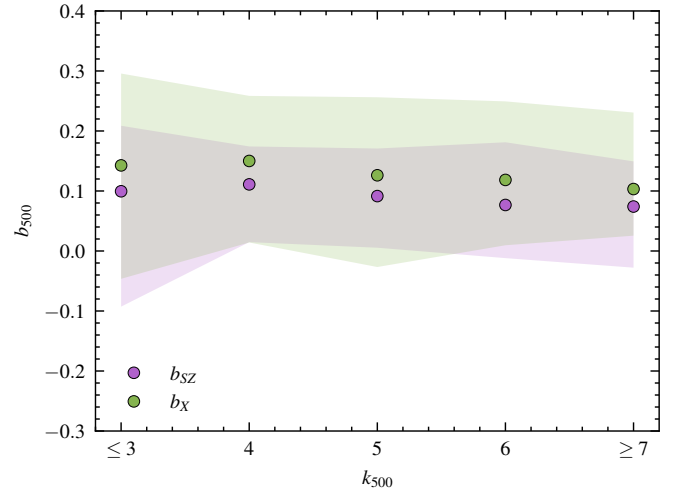

Fig. D.1. Connectivity and hydrostatic mass bias relation at redshift $z = 0$. In green are shown the mass bias median values, b_X, estimated at R_{500}, in violet the mass bias median values, b_{SZ}, at R_{500}. The shaded areas represent the 16th and 84th percentiles.